University of Groningen

The SAMI-Fornax Dwarfs Survey I: sample, observations, and the specific stellar angular momentum of dwarf elliptical galaxies

Scott, Nicholas; Eftekhari, F. Sara; Peletier, Reynier F.; Bryant, Julia J.; Bland-Hawthorn, Joss; Capaccioli, Massimo; Croom, Scott M.; Drinkwater, Michael; Falcón-Barroso, Jésus; Hilker, Michael

IMPORTANT NOTE: You are advised to consult the publisher's version (publisher's PDF) if you wish to cite from it. Please check the document version below.

Document Version
Publisher's PDF, also known as Version of record

Link to publication in University of Groningen/UMCG research database

The SAMI–Fornax Dwarfs Survey I: sample, observations, and the specific stellar angular momentum of dwarf elliptical galaxies

Nicholas Scott [1,2]★ F. Sara Eftekhari,[3] Reynier F. Peletier [3] Julia J. Bryant,[1,2]
Joss Bland-Hawthorn [1,2] Massimo Capaccioli,[4] Scott M. Croom [1,2] Michael Drinkwater [5]
Jésus Falcón-Barroso,[6,7] Michael Hilker,[8] Enrichetta Iodice,[9] Nuria F. P. Lorente,[10] Steffen Mieske,[11]
Marilena Spavone [9] Glenn van de Ven [12] and Aku Venhola[13]

[1]*Sydney Institute for Astronomy, School of Physics, A28, The University of Sydney, NSW, 2006, Australia*
[2]*ARC Centre of Excellence for All Sky Astrophysics in 3 Dimensions (ASTRO 3D)*
[3]*Kapteyn Institute, University of Groningen, Landleven 12, NL-9747, AD, Groningen, The Netherlands*
[4]*University of Naples Federico II, C.U. Monte Sant'Angelo, Via Cinthia, I-80126, Naples, Italy*
[5]*School of Mathematics and Physics, The University of Queensland, St Lucia, QLD 4072, Australia*
[6]*Instituto de Astrofísica de Canarias, Calle Vía Láctea s/n, E-38205 La Laguna, Tenerife, Spain*
[7]*Departamento de Astrofísica, Universidad de La Laguna (ULL), E-38206 La Laguna, Tenerife, Spain*
[8]*ESO, European Southern Observatory, Karl-Schwarzschild-Str 2, D-85748 Garching bei München, Germany*
[9]*INAF, Astronomical Observatory of Capodimonte, via Moiariello 16, I-80131 Napoli, Italy*
[10]*Australian Astronomical Optics, AAO-MQ, Faculty of Science and Engineering, Macquarie University, NSW 2109, Australia*
[11]*European Southern Observatory, Alonso de Cordova 3107, 7630355 Vitacura, Santiago, Chile*
[12]*Department of Astrophysics, University Vienna, Türkenschanzstrasse 17, A-1180 Wien, Austria*
[13]*Space physics and astronomy research unit, University of Oulu, Pentti Kaiteran katu 1, FI-90014 Oulu, Finland*

ABSTRACT
Dwarf ellipticals are the most common galaxy type in cluster environments; however, the challenges associated with their observation mean that their formation mechanisms are still poorly understood. To address this, we present deep integral field observations of a sample of 31 low-mass ($10^{7.5} < M_\star < 10^{9.5}$ M$_\odot$) early-type galaxies in the Fornax cluster with the SAMI instrument. For 21 galaxies, our observations are sufficiently deep to construct spatially resolved maps of the stellar velocity and velocity dispersion – for the remaining galaxies, we extract global velocities and dispersions from aperture spectra only. From the kinematic maps, we measure the specific stellar angular momentum λ_R of the lowest mass dE galaxies to date. Combining our observations with early-type galaxy data from the literature spanning a large range in stellar mass, we find that λ_R decreases towards lower stellar mass, with a corresponding increase in the proportion of slowly rotating galaxies in this regime. The decrease of λ_R with mass in our sample dE galaxies is consistent with a similar trend seen in somewhat more massive spiral galaxies from the CALIFA survey. This suggests that the degree of dynamical heating required to produce dEs from low-mass starforming progenitors may be relatively modest and consistent with a broad range of formation mechanisms.

Key words: galaxies: clusters: individual: Fornax – galaxies: dwarf – galaxies: evolution – galaxies: kinematics and dynamics.

1 INTRODUCTION

The population of low-redshift galaxies shows a clear bimodality between blue, star-forming, late-type galaxies and red, passive, early-type galaxies (e.g. Strateva et al. 2001). Understanding the physical processes that transform galaxies from star-forming to passive – so-called quenching mechanisms – is at the heart of studies of galaxy evolution.

Peng et al. (2010) argue that quenching can be separated into two distinct regimes: mass quenching and environment quenching. Mass quenching occurs when a galaxy's own halo prevents the formation of the dense gas necessary for star formation. Mass quenching operates on galaxies with stellar masses $M_* \gtrsim 10^{9.5}$ M$_\odot$, though it becomes efficient only at shutting down star formation at $M_* > 10^{11}$ M$_\odot$. Environment quenching occurs when a galaxy is influenced by factors outside its own halo – either nearby galaxies or its host group or cluster halo – in such a way as to cause star formation to cease. Environment quenching has an impact on galaxies of all masses but is efficient only in relatively dense environments and at low to intermediate galaxy masses.

A variety of environmental mechanisms have been proposed for quenching galaxies: ram-pressure stripping (Gunn & Gott 1972), strangulation (Larson, Tinsley & Caldwell 1980), harassment and tidal interactions (e.g. Hernquist 1989; Moore, Lake & Katz 1998), and merging. From studies of galaxies that are actively being

★ E-mail: nicholas.scott@sydney.edu.au

quenched (e.g. Koch et al. 2012; Poggianti et al. 2017; Jaffé et al. 2018; Owers et al. 2019; Zabel et al. 2019), we can identify signatures of the different quenching mechanisms in terms of differing time-scales and spatial distributions for the shut down of star formation (e.g. Schaefer et al. 2019). Most importantly for this work, we expect that ram-pressure stripping and strangulation will leave the stellar kinematics of a galaxy relatively undisturbed and cold (though Hammer et al. 2019, argue that sudden stripping may heat the kinematics in very low-mass galaxies), whereas harassment, mergers, and large tidal interactions will all serve to heat the kinematic distribution of the stars.

One limitation of this approach is that it focuses on only the small subset of galaxies that are undergoing quenching right now. From such targeted studies, it has been historically difficult to determine which physical processes play the most significant role in quenching galaxies. An alternative approach, and one better suited to address the demographics of quenching, is to study the large population of passive galaxies that have already quenched. We can potentially identify how the passive population was quenched by examining the kinematics, stellar populations, and gas content of quenched galaxies, a task ideally suited to integral field spectroscopy. Starting with the SAURON survey (Cappellari et al. 2007; Emsellem et al. 2007), large IFS surveys of giant ($M_\star \gtrsim 10^{9.5}$ $M_\odot$) passive galaxies have found two distinct kinematic classes of objects, slow rotators and fast rotators, based on their kinematic morphologies and specific stellar angular momentum. The Atlas^{3D} survey (Emsellem et al. 2011) found slow rotators to make up a significant proportion of the giant, passive galaxy population only for galaxies with $M_\star \gtrsim 10^{11}$ $M_\odot$. Below this mass, the vast majority of passive galaxies are fast rotators (see Cappellari 2016, for an overview). This trend has been confirmed by a series of IFS surveys with increasingly large sample sizes (van de Sande et al. 2017; Veale et al. 2017; Graham et al. 2018; Falcón-Barroso et al. 2019). In the Fornax cluster, Scott et al. (2014) examined the stellar kinematics of a subset of the most massive passive galaxies, finding only two slow rotators in the cluster, a result confirmed by the Fornax 3D survey (Sarzi et al. 2018; Iodice et al. 2019). Note that the fast rotator/slow rotator classification scheme was developed for galaxies with $M_\star \gtrsim 10^{9.5}$ $M_\odot$, and it is not clear that it is applicable to lower mass galaxies with significantly different formation histories.

Unfortunately, for massive galaxies in dense environments, both mass quenching and environment quenching are expected to contribute to the shut down of star formation, making the two independent processes difficult to separate. In contrast, for low-mass dwarf galaxies, environmental processes are expected to dominate, with mass quenching playing a negligible role in influencing their observed properties. This makes low-mass galaxies in dense environments ideal objects to study the mechanisms of environmental quenching. The low-mass population of galaxies in galaxy clusters is dominated by galaxies with a dwarf elliptical (dE) morphology – that is red, passive, spheroidal systems (Lisker et al. 2007; Janz et al. 2012; Roediger et al. 2017; Venhola et al. 2019), though they may exhibit a range of stellar population ages (Hamraz et al. 2019) and internal structures (Lisker, Grebel & Binggeli 2006). As predominantly passive objects (Roediger et al. 2017), dE galaxies represent one end result of the physical processes of environmental quenching.

The impact of environment on the quenching of dwarf galaxies has been widely studied using imaging and fibre spectroscopy. dEs are extremely rare in low-density environments (Geha et al. 2012; Davies et al. 2016), implying that the environment plays

a key role in shutting down star formation in dwarf galaxies. Both observations (Michielsen et al. 2008; Wetzel et al. 2013) and simulations (Boselli et al. 2008; Fillingham et al. 2015, 2016) suggest that the shut down of star formation occurs rapidly on time-scale of order 1 Gyr, with ram pressure stripping the leading mechanism (Boselli & Gavazzi 2014). Kinematic heating due to harassment may occur on longer time-scales (Michielsen et al. 2008; Benson et al. 2015). This scenario suggests that the progenitors of present-day dEs are low-mass, star-forming spiral and irregular galaxies (however, these progenitors may not be similar to present-day low-mass star-forming galaxies, see Lisker et al. 2013). An alternative formation scenario, where dEs represent the low-mass tail of the giant elliptical population, is suggested by consistent scaling relations between the two classes (e.g. Geha, Guhathakurta & van der Marel 2003; Chilingarian 2009); however, the strong environmental dependence of dE number density is difficult to reconcile with this scenario.

While common in galaxy clusters, the resolved kinematics of dEs are challenging to measure. They are intrinsically faint, have small effective radii, and are expected to have rotation velocities or velocity dispersions of, at most, a few 10 s of km s^{-1}. Despite these challenges, several recent studies have targeted dEs, predominantly in clusters, either with IFS (Ryś, Falcón-Barroso & van de Ven 2013; Adams et al. 2014; Mentz et al. 2016; Penny et al. 2016) or with long-slit spectroscopy (Pedraz et al. 2002; Toloba et al. 2014; Penny et al. 2015), including specifically in isolated environments (Janz et al. 2017). These studies find a variety of kinematic morphologies for dE galaxies, with an increase in the relative proportion of slow rotators compared to intermediate mass ($M_\star \sim 10^{10}$ $M_\odot$) galaxies. However, the sample size of these studies is modest compared to those of more massive galaxies – for the IFS studies, at most a dozen objects, and a few tens for the long-slit studies. They are also restricted to the brighter end of the dE distribution, primarily targeting galaxies with $M_\star > 10^9$ $M_\odot$.

In this work and a short series of following papers, we aim to address these two deficiencies in our current understanding of dEs by observing and analysing a new, large sample of low-mass galaxies in the nearby Fornax cluster. We cover a sample of dwarf galaxies representative of the general cluster dwarf population and exploring down to magnitudes and surface brightness that have not been studied before. Our sample offers the opportunity to study the dark matter content of dwarf galaxies with a potentially significant amount of dark matter in a mass regime that bridges observations of the Local Group dSph population and existing studies of more massive dwarf galaxies (e.g. Ryś, van de Ven & Falcón-Barroso 2014). Observations, described in Section 2, were undertaken using the Sydney Anglo Australian Observatory Multi-Object Integral Field Spectrograph (SAMI). We take advantage of deep, wide-field photometry from the Fornax Deep Survey (FDS, Iodice et al. 2016; Venhola et al. 2018) to select and characterize our targets, described in Section 3. We describe the reduction of the SAMI data in Section 4 and briefly describe the stellar kinematics analysis in Section 5, with details provided by Eftekhari et al. (in preparation). In Section 6, we present an analysis of the stellar kinematics of dE galaxies in the Fornax cluster and conclude in Section 8. Analysis of the integrated stellar kinematics of this sample is presented by Eftekhari et al. (in preparation), with an analysis of the stellar populations to appear in a future article.

Throughout this work, we adopt a distance to the Fornax cluster of 20.0 Mpc (Blakeslee et al. 2009) and a virial radius for the cluster of 2.2 deg (0.77 Mpc at our adopted distance, Drinkwater, Gregg & Colless 2001b).

2 OBSERVATIONS

All observations were conducted with the Sydney – Australian Astronomical Observatory (AAO) Multi-Object Integral-Field spectrograph (SAMI, Croom et al. 2012) on the 3.9-m Anglo-Australian Telescope at Siding Spring Observatory, New South Wales. SAMI is a fibre-fed, multiobject integral-field spectrograph that feeds the AAOmega spectrograph (Sharp et al. 2006).

SAMI uses the innovative 'hexabundle' technology (Bland-Hawthorn et al. 2011; Bryant et al. 2011, 2014), where individual optical fibres are fused together to make integral field units (IFUs). SAMI consists of 13 such IFUs, where each IFU consists of 61 individual 1″6 diameter fibres arranged in a close-packed pattern. The resulting hexabundles have an on-sky diameter of 15 arcsec, which can be placed anywhere within the instrument's 1-deg field of view. In addition to the 13 hexabundles, there are 26 dedicated sky fibres that are placed at pre-determined blank sky positions throughout the field of view to enable simultaneous observation of the night sky background.

The AAOmega spectrograph is a double-armed spectrograph covering the blue and red optical regions of the electromagnetic spectrum. AAOmega allows variable wavelength coverage and spectral resolution in each arm. For the SAMI–Fornax Dwarfs Survey, we used the 1500 V grating in the blue arm and the 1000 R grating in the red arm to provide high enough spectral resolution to measure velocity dispersions in low-mass galaxies. Note that this is different from the standard setup used by the SAMI Galaxy Survey (Allen et al. 2015; Green et al. 2018; Scott et al. 2018), which utilized the 580 V grating in the blue arm. This non-standard setup resulted in one fibre falling off the edge of the detector, leaving only 25 usable sky fibres.

For each observed field, 12 hexabundles were allocated to galaxy targets, with one hexabundle allocated to a secondary standard calibration star. This secondary standard star facilitates several critical steps in the data reduction (e.g. telluric correction, absolute flux calibration), as well as allowing us to assess the point spread function and transmission of each individual observation.

For each field, we aimed to obtain 7 h (∼25 000 s) of on-source integration time. Our observing strategy followed that of the SAMI Galaxy Survey (Sharp et al. 2015). Individual integrations were ∼1800 s, with dithers of 0″8 (half a fibre diameter) applied between exposures, following a seven-point hexagonal dither pattern, optimized for the SAMI hexabundles. The dither pattern ensures an even distribution of S/N over a hexabundle, accounting for the gaps between fibres. This seven-point dither pattern was repeated twice for each field, yielding $2 \times 7 \times 1800 \simeq 25\,000$-s total exposure time per galaxy. Arc lamp calibrations and observations of primary spectophotometric standard stars from the European Southern Observatory Optical and UV Spectrophometric Standard Stars catalogue[1] were interspersed with the object exposures at regular intervals.

Observations took place over three separate observing runs between 2015 and 2018. Table 1 provides an overview of the three observing runs, with the mean seeing and mean exposure time per field for each run.

In 2015, observing was significantly affected by poor weather, resulting in only two fields being successfully observed. Four targets suffered from inaccurate catalogue coordinates, falling partially or

[1]Available at: https://www.eso.org/sci/observing/tools/standards/spectra.html.

Table 1. Summary of SAMI–Fornax Survey observing runs.

Date	Fields observed	Median seeing	Exposure Time per Field (h)
4th–8th Nov 2015	2	2.3 arcsec	7.0
26th–30th Oct 2016	3	1.9 arcsec	6.7
9th– 5th Oct 2018	5	2.2 arcsec	6.1

entirely outside their allocated hexabundle field of view. Observations in 2016 and 2018 were not affected by inaccurate coordinates due to the improved FDS input catalogue and all targets filled their allocated bundles. The weather was somewhat improved in 2016 and 2018, allowing a higher fraction of target fields to be observed during those runs. Over the three observing runs, we observed 10 complete fields, totalling 118 unique galaxies.

3 SAMPLE

Our primary science targets consist of morphologically classified dE galaxies in the Fornax cluster. Due to the on-sky density of primary targets, not all IFUs could be allocated to a dE for each observation. Spare IFUs were allocated to other dwarf galaxies, giant cluster members of any morphological type, or background galaxies in that order of preference. In practice, a target catalogue was prepared for each semester, and targets were assigned priorities ranging from 5 (highest) to 1 (lowest) as described below. A tiling algorithm (Bryant et al. 2015) then assigned targets to fields in a way that maximizes the number of high priority targets observed while also ensuring that all IFUs have an available target.

Targets were selected from the Fornax Cluster Catalogue (Ferguson & Sandage 1990, hereafter FCC) for observations in 2015, and from the FDS catalogue (Venhola et al. 2018, hereafter FDS) in 2016 and 2018, once this deeper, wider-field photometry became available. In the following subsections, we provide details of how targets were selected for each observing run and the properties of the final sample of observed objects. Primary and secondary targets, and their positions within the cluster are shown in Fig. 1.

3.1 Fornax Cluster Catalogue selection

In 2015, we selected primary science targets from the FCC because higher fidelity catalogues with all required information were not yet available. We selected galaxies within a 3×1 deg region centred on the cluster centre, which we assume is coincident with the centre of NGC 1399, the Brightest Cluster Galaxy in Fornax. We included only galaxies with a membership class of 1 (definite member) or 2 (likely member) in the FCC. This resulted in an input catalogue of 82 galaxies.

Priorities were assigned based on the absolute B-band magnitude of the targets and the observed morphology but were adjusted to prioritize potentially interesting objects. Galaxies with a dE or dS0 morphology and $-18 < M_B \leq -13$ were assigned the highest priority 5 (31 objects), with fainter ($-11 < M_B < -13$) dE- and dS0-assigned priority 4 (31 objects). Relatively compact galaxies (effective radii less than the bundle diameter of 15') not satisfying either of the above criteria were assigned priority 3 (eight objects), with the remaining massive early-types and late-type galaxies of all magnitudes assigned priorities 1 and 2 (12 objects). Note that these numbers refer to galaxies in our input target catalogue; the galaxies that were actually selected are described in Sections 3.2 and 3.3.
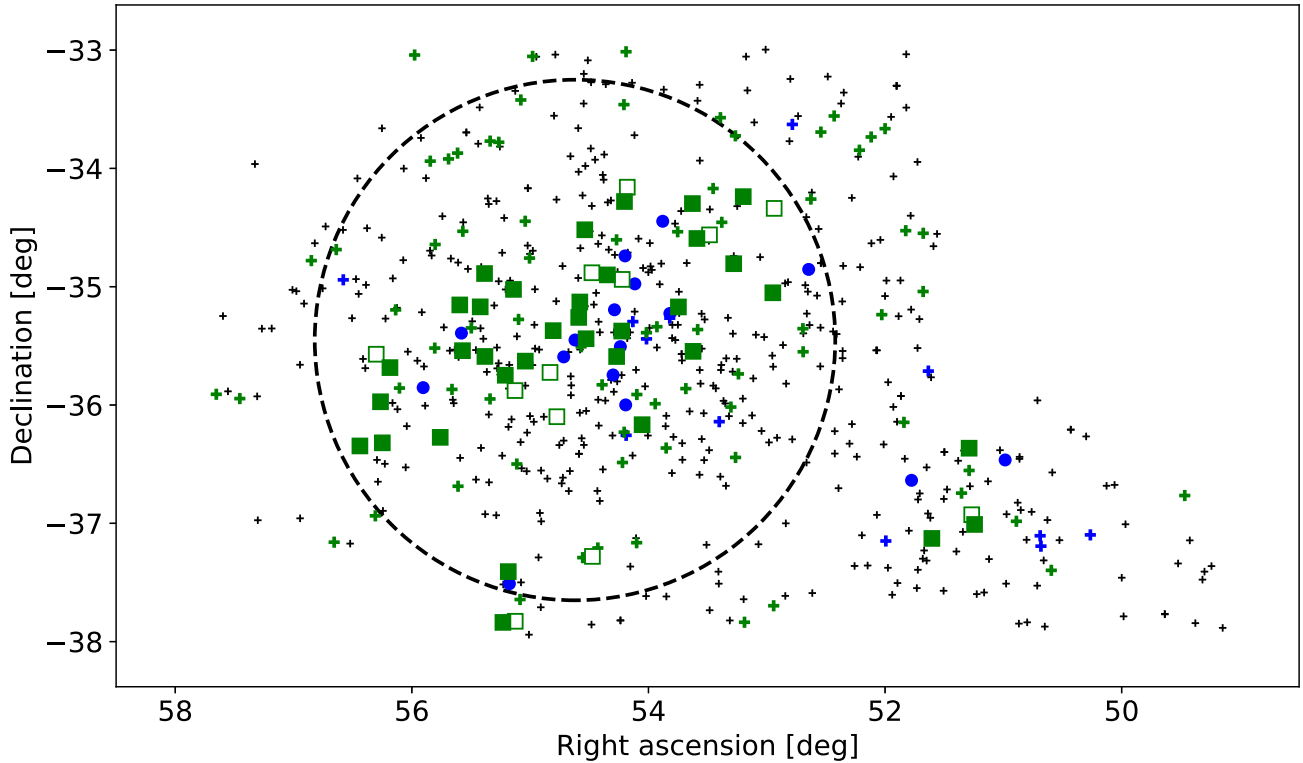
Figure 1. Map of galaxy positions within the Fornax cluster. Filled green squares indicate primary targets with successful stellar kinematic measurements, and open green squares primary targets without stellar kinematic measurements. Blue circles indicate giant galaxies with kinematic measurements. Blue and green crosses indicate, respectively, giant and primary galaxies that were not observed by SAMI. Small black crosses indicate low-mass dwarf galaxies. All positions for galaxies in the FDS are taken from Venhola et al. (2018). The dashed line indicates the cluster Virial radius of 2.2 deg (Drinkwater et al. 2001b).

3.2 Fornax Deep Survey selection

The selection and prioritization of targets from the FDS were similar to that from the FCC, with modifications based on experience from the 2015 observations and to take advantage of the improved quality and quantity of the FDS catalogue compared to the FCC.

We began by selecting all galaxies in the FDS catalogue with $-14 > M_r > -19$ and $\mu_r < 23.5$ and a dE visual morphology (from the FCC). The surface brightness criterion selected against galaxies for which we were unable to obtain useful data in the 2015 observations (S/N <10 integrated over the entire galaxy). Galaxies with $M_r > -14$ were not included, even as lower priority targets, again based on our experience from the 2015 observations on which targets yielded useful spectra. Secondary targets consisted of giant galaxies with $M_r < -19$, dwarf galaxies with a non-dE morphology, and an additional sample of ultra-compact dwarf galaxies (UCDs) from Wittmann et al. (2016). We also included galaxies identified as unlikely cluster members or background galaxies as low-priority secondary targets.

In 2016, FDS coverage of the cluster was incomplete, so we selected targets from the central ∼1 deg for which the catalogue was already complete. Prior to the 2018 observations, the FDS catalogue had been extended to cover the outer regions of the cluster, allowing us to target regions further from the cluster centre. In 2018, we observed regions between 1 and 3 deg from the cluster centre with sufficient galaxy density to assign the majority of hexabundles to a primary dE target.

Priorities were assigned to targets in a similar fashion as for the 2015 FCC sample. Galaxies with a dE morphology, $-14 > M_r >$

-19 and $\mu_r < 23.5$ were assigned priority 5 (the highest priority). UCDs were assigned priority 4 and dwarf galaxies with a non-dE morphology were assigned priority 3. Giant galaxies were assigned priority 2, with background galaxies assigned priority 1. As before, targets were assigned to fields by the tiling algorithm to maximize the number of high-priority targets observed.

3.3 Primary sample

As noted above, our primary science targets were galaxies with a dE or dS0 morphology and $M_r > -19$. Of the 118 galaxies targeted, 59 (50 per cent) fall into this category. A complete list of low-mass, early-type galaxies with successful stellar kinematic measurements can be found in Table 2. Here, we describe the properties of this primary sample and compare to the full FDS catalogue to identify possible bias in our observed sample with respect to the complete cluster population. We also examine the distribution of observed galaxies within the Fornax cluster to highlight the environmental coverage of this sample, again with respect to FDS.

Fig. 2 shows the $(g - r)$ versus M_g colour–magnitude diagram for our sample (green circles) and for the full FDS sample (blue crosses). Filled and open green symbols indicate galaxies where our stellar kinematic measurements were successful or unsuccessful, respectively (see Section 5 for details). As we are primarily interested in galaxies with an early-type morphology, it is unsurprising that the majority of our targets fall on the red sequence for the cluster;

Table 2. SAMI–Fornax Dwarfs Survey dwarf galaxies with successful stellar kinematic measurements, ordered by decreasing $M_\star$.

FDS ID	FCC ID	RA (deg)	Dec (deg)	M_r (mag)	M_g (mag)	R_e (arcsec)	$\log M_\star$ ($M_\odot$) (1)	Morph. Class (2)	ϵ	λ_{R_e} (3)	Max rad (R_e) (4)
Dwarf ellipticals
6_D002	277	55.59492	−35.1541	−18.8	−18.1	11.4	9.47	e(s)	0.42	0.27	0.95
16_D002	143	53.7466710	−35.171061	−18.6	−18.0	9.8	9.45	e(s)	0.15	0.15	1.1
7_D000	301	56.2649	−35.97267	−18.3	−17.7	7.6	9.36	e(s)	0.46	0.39	1.6
11_D279	182	54.2262696	−35.374677	−17.9	−17.1	9.7	9.16	e(s)∗	0.04	0.18	1.05
16_D159	136	53.6227783	−35.546452	−17.8	−17.0	17.5	9.08	e	0.15	0.15	0.65
11_D235	202	54.5266666	−35.43833	−17.3	−16.6	13.3	8.90	e∗	0.41	0.13	0.85
15_D417	106	53.19867	−34.23873	−17.4	−16.8	10.7	8.89	e(s)	0.51	0.14	1.15
11_D283	222	54.8054166	−35.36972	−17.0	−16.3	16.1	8.77	e∗	0.11	0.32	0.6
10_D189	203	54.5381730	−34.518726	−16.9	−16.3	16.0	8.75	e(s)	0.45	0.33	0.75
15_D384	135	53.6285240	−34.297455	−16.8	−16.2	14.7	8.70	e(s)	0.53	0.31	0.75
16_D417	100	52.94848	−35.05139	−17.0	−16.2	19.8	8.70	e∗	0.24	0.28	0.55
11_D069	252	55.20999	−35.74846	−16.4	−15.7	11.1	8.58	e∗	0.06	0.15	0.8
11_D458	245	55.14099	−35.02289	−16.5	−15.8	14.5	8.57	e∗	0.08	0.19	0.65
7_D326	300	56.24959	−36.31975	−16.4	−15.7	20.8	8.55	e∗	0.28	0.28	0.55
11_D396	207	54.5795833	−35.1275	−16.6	−16.0	9.6	8.51	e	0.17	0.31	0.85
6_D455	266	55.42216	−35.17027	−16.3	−15.7	6.9	8.49	e∗	0.11	0.17	1.35
11_D155	188	54.26875	−35.58861	−16.2	−15.5	12.2	8.42	e∗	0.04	0.20	0.8
11_D339	211	54.58875	−35.25833	−16.1	−15.5	6.6	8.33	e∗	0.25	0.11	1.5
12_D367	164	54.0537009	−36.166437	−16.0	−15.4	9.9	8.33	e(s)	0.45	0.08	1.15
11_D079	223	54.83125	−35.72333	−16.1	−15.5	17.0	8.32	e∗	0.11	–	–
13_D042	253	55.2303	−37.83763	−15.8	−15.1	10.9	8.30	e	0.38	0.26	1.0
6_D208	274	55.5716666	−35.53916	−15.7	−15.2	12.0	8.17	e∗	0.04	–	–
6_D098	298	56.18507	−35.68372	−15.6	−15.0	7.0	8.16	e∗	0.29	0.18	1.5
10_D014	195	54.3471331	−34.900098	−15.4	−14.8	12.8	8.13	e	0.46	–	–
6_D170	264	55.3820833	−35.58777	−15.5	−14.9	10.3	8.09	e	0.60	–	–
13_D258	250	55.18497	−37.40827	−15.1	−14.4	9.2	7.97	e	0.24	–	–
10_D302	178	54.2027295	−34.280105	−15.0	−14.5	11.3	7.95	e	0.29	–	–
15_D232	B904	53.4840889	−34.561798	−15.2	−14.6	5.1	7.90	e	0.20	–	–
10_D003	181	54.2219391	−34.938393	−15.0	−14.3	9.7	7.87	e∗	0.40	–	–
15_D223	134	53.5904080	−34.592517	−14.6	−14.1	6.5	7.63	e	0.43	–	–
21_D129	B442	51.77604	−36.63679	−14.1	−13.6	4.5	7.59	e	0.30	–	–
Star forming dwarfs (spirals and irregulars) with $M_r > -19$
26_D003	33	51.24324	−37.00961	−18.1	−17.4	16.9	9.24	l	0.63	0.46	0.75
11_D519	235	55.041069	−35.629093	−18.6	−18.2	42.3	9.03	l	0.32	–	–
25_D241	37	51.2893372	−36.365185	−18.2	−17.8	33.9	9.02	l	0.32	–	–
5_D000	263	55.38557	−34.88875	−18.3	−17.7	16.5	9.00	l	0.52	0.15	0.75
7_D360	285	55.7601471	−36.273358	−18.0	17.5	32.7	8.78	l	0.26	–	–
15_D17	113	53.279419	−34.805576	−17.0	−16.5	18.9	8.48	l	0.31	–	–
22_D244	46	51.6043	−37.12778	−16.3	−15.8	8.5	8.31	l	0.36	0.38	1.3
7_D310	306	56.43909	−36.3461	−15.9	−15.5	7.2	7.91	l∗	0.41	0.52	1.6

Note. Unless otherwise stated, all values are taken from the FDS dwarf catalogue (Venhola et al. 2019). (1) Stellar masses are determined following Taylor et al. (2011), using the observed $(g - i)$ colour and r-band absolute magnitude. (2) Visual morphological classes from Venhola et al. (2019): e = smooth early-type, l = smooth late-type, ∗ = nucleated, (s) = structured. (3) λ_R measured within a 1 R_e aperture, or, where the kinematics do not extend to 1 R_e, derived from aperture-correcting λ_R within the largest available aperture. The typical uncertainty on λ_{R_e} is ∼5 per cent. (4) Maximum extent of the stellar kinematics, as a fraction of R_e.

however, we also target a number of blue objects, where they satisfy our selection criteria.

In Fig. 3, we show the distribution in surface brightness for our full observed sample (open green histogram) and the subset for which we are able to measure stellar kinematic measurements (filled green histogram, see Section 5 and Eftekhari et al. in preparation for details). The pale blue histogram shows the complete FDS galaxy sample from Venhola et al. (2018). Below an effective surface brightness of $\mu_r = 23.5$, we are unable to measure stellar kinematics; therefore, in the following section, we consider only galaxies with $\mu_r < 23.5$. We restrict this comparison to our primary targets only, with $-19 < M_r < -14$.

In Fig. 4, we show the distribution in a range of galaxy properties of SAMI–FDS primary targets. With respect to the subset of the FDS sample consistent with our revised selection criteria ($\mu_r < 23.5$, $-19 < M_r < -14$), our primary sample is more massive than the full FDS sample, driven by a decrease in our completeness below $M_* = 10^8 M_\odot$. This is particularly true for the subset of galaxies for which we have successful stellar kinematic measurements, unsurprising due to the relatively high S/N required to obtain spatially resolved spectroscopy. The R_e distribution of the SAMI–FDS primary sample is consistent with that of the full FDS sample. Our sample is redder and rounder and has slightly higher Sérsic index n than the full FDS
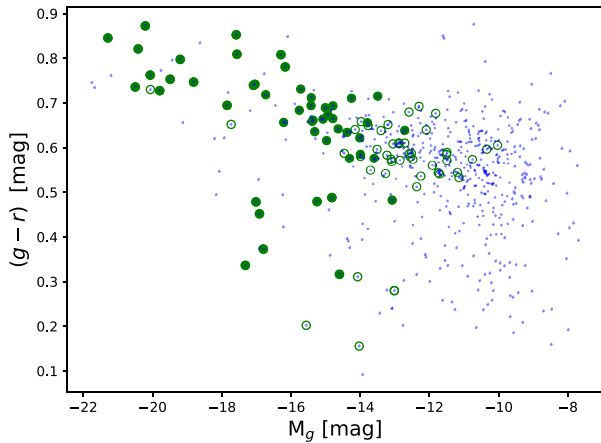
Figure 2. The $(g - r)$ versus M_g colour-magnitude diagram for our sample (green circles), compared to that from the full FDS sample (blue crosses). We primarily target galaxies on the red sequence but do include some blue galaxies that satisfy our selection criteria. Filled (open) symbols indicate galaxies for which we could (could not) obtain aperture stellar kinematic measurements.
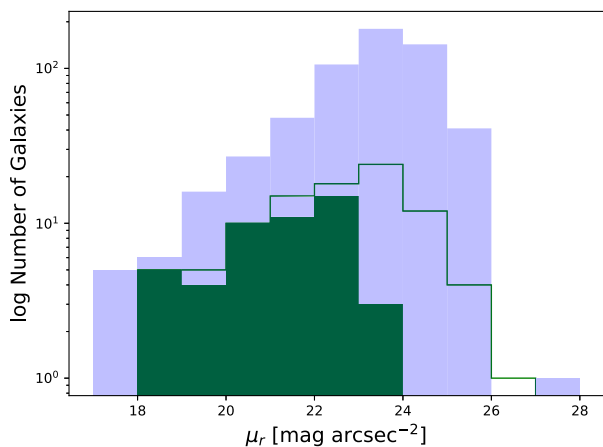

Figure 3. The logarithm of the number of galaxies as a function of effective surface brightness. The open green histogram shows the distribution for all observed SAMI–FDS galaxies, while the solid green histogram indicates only those for which we were successful in measuring stellar kinematics. The pale blue histogram indicates the effective surface brightness distribution for the full FDS sample.

sample, reflecting our primary sample selection criteria of targeting galaxies with an early-type morphology.

In summary, while the galaxies for which we successfully obtain stellar kinematic measurements are, on average, more massive, rounder, and redder than FDS dwarf galaxies, our sample is representative of bright, early-type dwarf galaxies in the FDS, in the sense that the fractional completeness of the SAMI–FDS galaxies with stellar kinematics is independent of the examined galaxy properties in the mass regime $M_* > 10^8 \, M_\odot$.

3.4 Secondary targets

In addition to our primary science targets, we observed 59 secondary targets. These objects consist of faint early-type cluster members (11 objects), giant early-type cluster members (14 objects), late-type

cluster members (14), UCDs (five objects), and background galaxies (15 objects). Late-type dwarf galaxies for which we could measure stellar kinematics are included in Table 2, while the remaining secondary targets can be found in Table B1 of the online appendices. These objects were not selected in any systematic fashion but instead were drawn randomly from targets that could be allocated to an IFU while maximizing the number of primary targets observed. Because of this, we do not attempt to quantify their sample properties with respect to any parent distribution but instead simply provide an overview. Secondary targets are not included in the subsequent analysis.

4 DATA REDUCTION

Our SAMI observations were reduced using the *sami* PYTHON package (Allen et al. 2015), following the approach described in Scott et al. (2018), with further details provided in Sharp et al. (2015) and Green et al. (2018). Here, we summarize this process and provide a detailed description only where our reduction process differed from that described in the above articles.

SAMI data are reduced in two stages: the first takes the data from raw observed frames to Row-Stacked Spectra (RSS) frames, which is handled primarily by the 2-deg field data reduction software package 2DFDR.[2] The second stage takes the data from RSS frames to flux-calibrated, three-dimensional data cubes, utilizing purpose-built PYTHON software as part of the *sami* package. The entire process is overseen by the *sami* PYTHON *manager*.

Data reduction with 2DFDR includes the standard steps of bias subtraction, flat-fielding, wavelength calibration, and sky subtraction. In addition, spectra corresponding to individual fibres are extracted using 'tramlines' fit to observations of the twilight sky. Subsequent to the fibre extraction, telluric correction and relative and absolute flux calibration steps are applied utilizing the spectrophotometric standard star and secondary standard star observations. Finally, the data for each individual object are extracted from the RSS frames and combined into a three-dimensional data cube using a drizzle-based algorithm.

During the 2015 observing run, it was discovered that the tramlines for the 1500 V grating were not well aligned to the CCD, resulting in one- or two-fibre spectra partially falling off the edge of the CCD – this primarily affected one sky fibre, but in three observations in 2016, an outer fibre from the first hexabundle was also affected. The influence on the output data quality is essentially negligible: the resultant decrease in the S/N of the sky spectrum is only 2 per cent, and the reduction in area of the first hexabundle (when it is affected) is only 1.5 per cent. This does not affect the 1000 R red arm observations or observations with the more widely used 580 V blue arm grating.

SAMI's circular fibre spectra are resampled on to a regular, square grid using a drizzle algorithm. There are two free parameters in this algorithm, the size of the square output spaxels and the drop factor, which effectively shrinks the size of the SAMI fibre before determining which output spaxels receive flux from a circular fibre. The SAMI Galaxy Survey adopted an output spaxel size of 0″.5 and a drop factor of 0.5, yielding an effective fibre diameter of 0″.8. Due to the lower effective surface brightness of the dwarf galaxies observed in this study, we adopted an output spaxel size of 1 arcsec (which corresponds to 97 pc at the adopted Fornax distance), increasing the flux per spaxel. While this comes at the cost of reduced spatial resolution, the Fornax cluster is 10 times closer than typical for the
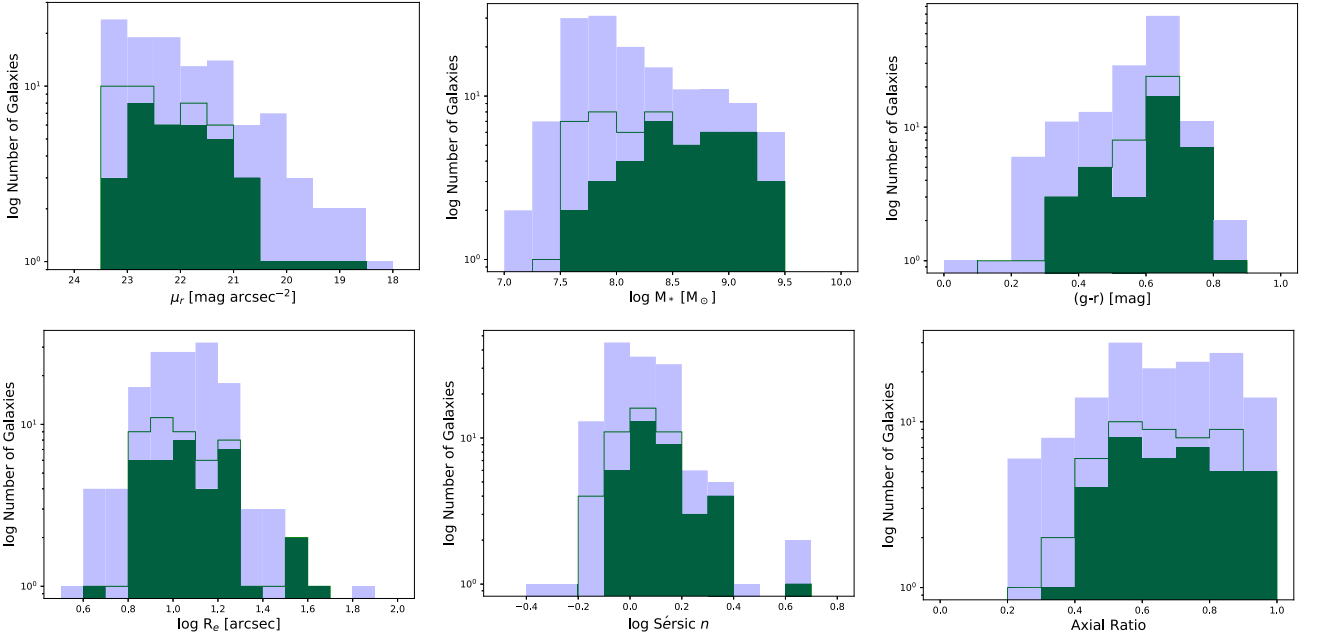
---

[2]https://www.aao.gov.au/science/software/2dfdr

Figure 4. Distribution of observed (open green), stellar kinematics (filled green), and FDS (pale blue) galaxies that satisfy our primary sample selection criteria (see text for details) with respect to a range of galaxy properties. Top row: r-band effective surface brightness, stellar mass, and $(g - r)$ colour. Bottom row: effective radius, Sérsic n, and axial ratio (b/a).

SAMI Galaxy Survey, resulting in much higher physical resolution, despite the larger spaxels.

5 STELLAR KINEMATICS

In the following section, we present stellar kinematic maps of galaxies in our primary sample with sufficiently high S/N to produce reliable maps. The stellar kinematic measurements are fully described in Eftekhari et al. (in preparation), but we briefly summarize them here.

The data cubes were spatially binned to a median S/N of at least 10 in the blue continuum, averaged over the wavelength range of 4900–5100 Å, using the Voronoi binning algorithm of Cappellari & Copin (2003). The binned spectra were analysed using the penalized Pixel Fitting (pPXF) software of Cappellari & Emsellem (2004). For spectral templates, we utilized a subset of the ELODIE (Prugniel et al. 2007) stellar spectral library, as this is the empirical library best matched to the SAMI 1500 V spectral resolution. Emission features were masked before extracting the moments of the mean line-of-sight velocity distribution: velocity (V) and velocity dispersion. The spatially resolved measurements of V and σ were used to construct the maps presented and analysed in the following section.

6 RESULTS

6.1 Stellar kinematic maps

In Fig. 5, we present the velocity and velocity dispersion maps (and r-band cutout images from FDS) for two example galaxies in our primary sample with good-quality stellar kinematics (with the full set of maps presented in Figures A1 and A2 of the online appendices). 'Good quality' here refers to maps for which the spectral fits to all

spaxels appear good, as judged by visual inspection, and represents a very conservative selection. For kinematic measurements of fainter galaxies and a detailed examination of the measurement uncertainties, see Eftekhari et al. (in preparation). Maps for secondary targets are presented in Figure B1 of the online appendices. Galaxies in our sample show a range of kinematic morphologies from strong, ordered disc-like rotation to non-rotating and dispersion dominated. In Section 6.2 below, we quantify the relative angular momentum of our sample using the λ_R parameter.

There are a small number of objects that overlap between our primary sample and that of Iodice et al. (2019, from the Fornax 3D survey), with larger overlap with our secondary targets. Noting the significant differences in radial coverage and instrumental resolution between the two studies, we find excellent agreement between the velocity and velocity dispersion maps of that work and those presented here. A more detailed quantitative comparison between the two sets of measurements will be presented in Eftekhari et al. (in preparation).

6.2 λ_R measurements

Emsellem et al. (2007) introduced the specific stellar angular momentum proxy, λ_R, as a parameter to quantify whether a galaxy is dominated by rotational or pressure support. λ_R is similar to the common $(V/\sigma)_e$ parameter but is more closely related to the kinematic morphology of a galaxy. λ_R is defined as:

$$\lambda_R = \frac{< R|V| >}{< R\sqrt{V^2 + \sigma^2} >} = \frac{\sum_{i=0}^{N} F_i R_i |V_i|}{\sum_{i=0}^{N} F_i R_i \sqrt{(V_i^2 + \sigma_i^2)}}, \quad (1)$$

where the summation is over all i spaxels under consideration. F_i, V_i, and σ_i, respectively, refer to the flux, velocity, and velocity dispersion of the ith spaxel. In this work, R_i refers to the elliptical radius of the ith spaxel – that is the major axis radius of the ellipse on which the
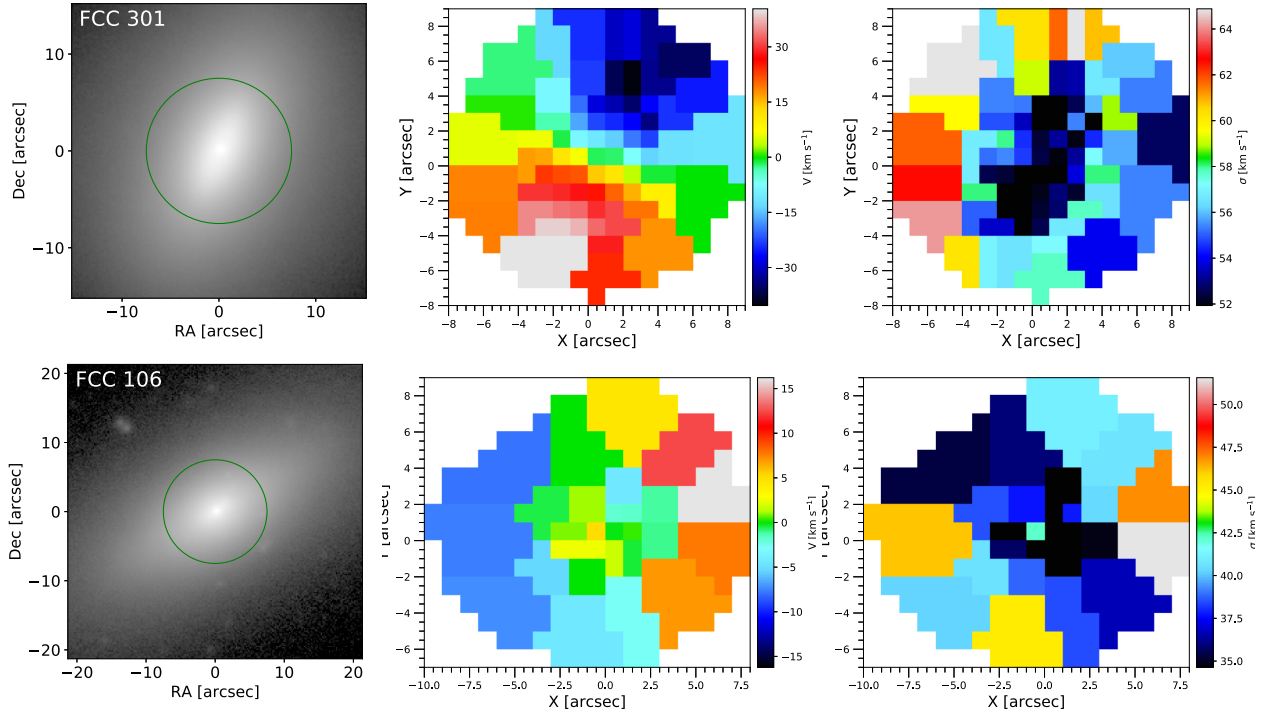
Figure 5. Stellar kinematic maps for two-example dE galaxies. Upper row: FCC301, a galaxy exhibiting strong, ordered rotation. Lower row: FCC106, a dispersion-dominated system with minimal rotation. Left column: *r*-band cutout images from FDS, with diameter 4 R_e. Green circle indicates the approximate position of the SAMI IFS field of view. Centre column: Voronoi-binned maps of the mean line-of-sight stellar velocity, *V*. Right column: Voronoi-binned maps of the mean line-of-sight stellar velocity dispersion, σ.
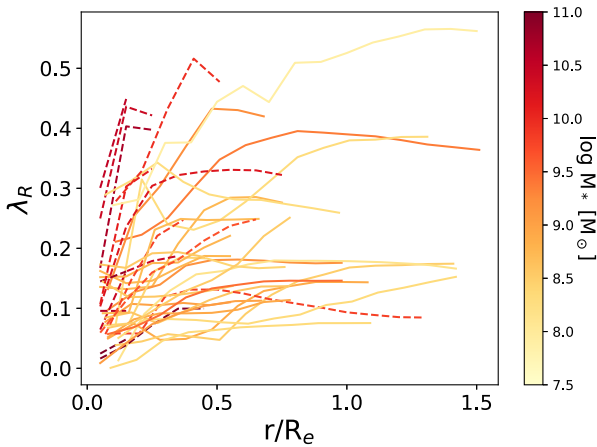
Figure 6. Profiles of λ_R (integrated within elliptical apertures of increasing radius) versus the radius of the corresponding aperture for all galaxies for which we could derive kinematic maps. Profiles are colour coded by the stellar mass of the galaxy. Solid lines indicate primary dE targets and dwarf late-types, dashed lines indicate giant galaxies.

*i*th spaxel lies, where the ellipticity, ϵ, and the position angle of the ellipse are taken from Venhola et al. (2018). Following van de Sande et al. (2017), for each spaxel, we set V_i and σ_i to the *V* and σ of the bin to which it belongs, whereas F_i is simply the unbinned flux of each spaxel.

λ_R is an integrated quantity measured within an aperture, or a series of increasing apertures to create a profile. In Fig. 6, we show

the λ_R profiles as a function of the normalized radius, r/R_e, coloured by the stellar mass of the galaxy. Solid lines indicate primary sample galaxies, while dashed lines indicate all secondary targets for which we were able to measure kinematics (primarily giant galaxies and more massive late-type dwarfs).

6.2.1 Aperture correction of λ_R

For all primary targets, our λ_R measurements sample out to at least $R_e/2$, with a median coverage of 0.85 R_e. Given this coverage range, we adopt R_e as our canonical aperture in which we measure λ_R. For galaxies where our kinematic measurements do not reach 1 R_e, we apply an aperture correction from van de Sande et al. (2017, their equations 7 and 10). We verify this aperture correction using the nine galaxies with λ_R measurements that extend beyond 1 R_e, finding that the corrected λ_R measurements are consistent with the measured λ_{R_e}, with a mean offset $\Delta(\lambda_R) = 0.01$ and rms scatter $\sigma(\lambda_R) = 0.04$. The median correction in λ_R for galaxies whose measurements do not reach 1 R_e is $\Delta(\lambda_R) = 0.04$.

The $\lambda_R - \epsilon$ plane is used to account for projection when comparing the specific stellar angular momentum of galaxies. It was first proposed by Emsellem et al. (2007) and represents a revision of the classical $V/\sigma - \epsilon$ diagram that has traditionally fulfilled this role. In Fig. 7, we show λ_{R_e} versus ϵ for our sample, coloured by the stellar mass of each galaxy, and with filled and open symbols indicating the primary sample and secondary targets, respectively. We explicitly choose not to apply one of the common criteria to divide galaxies into slow rotators and fast rotators in this plane (Emsellem et al. 2007, 2011; Cappellari 2016) as this classification was motivated
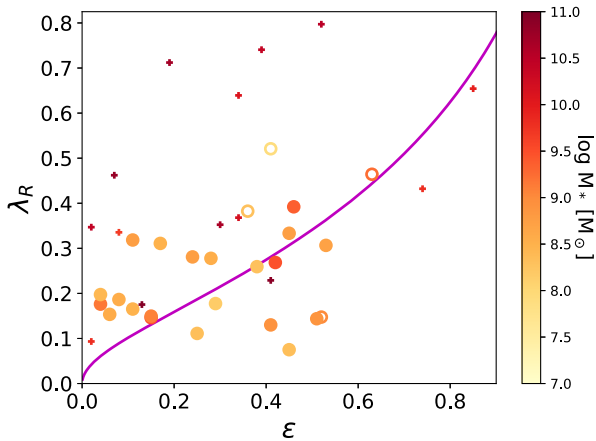
Figure 7. The λ_R versus ϵ plane for all galaxies for which we could derive kinematic maps. Points are colour coded by the stellar mass of the galaxy, with filled circles indicating primary dE targets, open circles late-type dwarfs, and small crosses giant cluster members. The magenta line indicates the model prediction for an edge-on axisymmetric galaxy from Cappellari et al. (2007) (see van de Sande et al. 2017, for further details).

by the properties of the giant galaxy population, and the utility of applying the same separation to dwarf galaxies is unclear.

7 DISCUSSION

7.1 The specific stellar angular momentum of dE galaxies

Naab et al. (2014) showed that for massive early-type galaxies, the position of a galaxy within the $\lambda_R - \epsilon$ plane correlates with its formation history, with galaxies at low λ_R typically having merging play a larger role in their evolution than galaxies at higher values of λ_R. For these massive galaxies, a number of studies have examined the distribution of the galaxy population in the $\lambda_R - \epsilon$ plane (e.g. Emsellem et al. 2011; van de Sande et al. 2017; Veale et al. 2017; Graham et al. 2018; Falcón-Barroso et al. 2019), noting a significant dependence on stellar mass. Ryś et al. (2013) extended this analysis to a small sample of dwarf galaxies in the Virgo cluster, finding a broader range in the degree of rotational support than in intermediate-mass early-type galaxies. Using long-slit spectroscopy, Toloba et al. (2014) obtained a significant sample of dwarf early-type galaxies, finding that in general, the rotational support in dEs is lower than in intermediate mass early-type galaxies, a result further supported by Janz et al. (2017). Here, we extend this analysis of dE galaxies to lower masses using our sample of dEs with spatially resolved stellar kinematic measurements.

In Fig. 8, we show the dependence of λ_R on $M_\star$ for early-type galaxies spanning nearby four orders of magnitude in stellar mass. We combine data from this study with more massive Virgo dwarf galaxies from Toloba et al. (2015, including a correction from long-slit to IFS-equivalent values using their equation 3) and isolated dwarfs from Janz et al. (2017). We include only our primary dE targets here because (i) the aperture corrections for the giant early types observed in this study are large and relatively uncertain, and (ii) those galaxies were selected in a way that is not necessarily representative of the giant early-type population. For the Janz et al. (2017) sample (orange points), we show two values for each galaxy, indicating the range of values given by their model fits to long-slit data. We supplement these dwarf samples with early-type giants from Emsellem et al. (2011, both Virgo and field) and van de Sande et al. (2017, field

only). All samples are corrected to a 1 R_e aperture measurement following van de Sande et al. (2017). For the giant population, λ_R increases with decreasing $M_\star$, reaching a peak around $M_\star \sim 10^{10.25}$. Below this mass, we find that λ_R decreases with decreasing stellar mass. Low-λ_R, slowly rotating galaxies dominate both the very high ($M_\star > 10^{11.2}$ $M_\odot$) and low ($M_\star < 10^{8.5}$ $M_\odot$) mass regimes. At high masses, the transition to a slow rotator-dominated population as $M_\star$ increases is quite sudden (see Cappellari 2016), but at low masses, the decline in λ_R with $M_\star$ is relatively smooth.

We note that the samples used here have very different selection criteria and so interpreting the mean trend is challenging. Janz et al. (2017) selected early types based on having a quiescent stellar population, whereas the other studies select early types based on visual morphology, perhaps accounting for the typically lower λ_R of the Janz et al. (2017) galaxies. More significantly, the samples used here are drawn from quite different environments. This work and Toloba et al. (2014) consist entirely of galaxies in clusters; the sample of Emsellem et al. (2011) includes both cluster and field galaxies and that of van de Sande et al. (2017) and Janz et al. (2017) include no cluster galaxies but a mixture of group and field objects. We separate the sample into cluster and non-cluster galaxies and derive the mean λ_R as a function of mass for the two environments (dashed and dotted lines in Fig. 8). The behaviour is consistent in both the high- and low-density environments, with the mean λ_R falling at both high and low masses.

The trend of decreasing λ_R with decreasing $M_\star$ described above is consistent with Falcón-Barroso et al. (2019), who find a similar dependence of λ_R with $M_\star$ in a sample with a mix of morphologies. That we find this trend in a pure early-type sample shows that the variation in λ_R must be driven by stellar mass and cannot be attributed purely to the changing morphological mix of the galaxy population with stellar mass. Although the sample of Falcón-Barroso et al. (2019), shown in Fig. 9, only reaches masses of $\sim 10^9$ $M_\odot$ and is incomplete at the lowest masses, a clear decrease is seen in λ_R with decreasing $M_\star$ below $M_\star \sim 10^{10}$ $M_\odot$.

All of their faint galaxies are spirals, classified by them as Sc and Sd, with the average λ_R lower for Sds than for Scs. Falcón-Barroso et al. (2019) find that their late-type spirals have surprisingly low λ_R values for spiral galaxies. The systems with λ_R between 0.35 and 0.6 are typically edge-on systems, as they say. To keep these objects thin, such galaxies would need a considerable amount of dark matter (with the enclosed dynamical mass being a factor of 10 higher than the baryonic mass).

Here, we can add some more pieces to the puzzle. The objects in this paper have, in general, lower λ_R values than the galaxies of Falcón-Barroso et al. (2019), as expected by the trend in mass. The objects with $\lambda_R < 0.3$, i.e. the slowly rotating dEs, are generally not irregular and not face-on, indicating that they are genuinely dynamically hot systems, suggesting that the low-mass spirals of Falcón-Barroso et al. (2019) with low λ_R may also be dynamically hot, even though they are spirals. The dark matter fractions in our galaxies are also found to be higher than for intermediate-mass galaxies (Eftekhari et al. in preparation).

While low-mass spiral and irregular galaxies show lower values of λ_R than massive spirals (Falcón-Barroso et al. 2019), there remains a modest offset between the λ_R of dEs and Sc/Sd galaxies at fixed stellar mass. Ryś et al. (2014) show that the dynamics of dE galaxies in the Virgo cluster are consistent with their progenitors being comparable mass spiral galaxies that are tidally heated by the cluster environment. It is unclear whether the same argument can be extended to the lower mass dEs in this study as no comparison sample of Sc/Sd/Irr galaxies with masses $M_\star < 10^9$ $M_\odot$ exists. If the
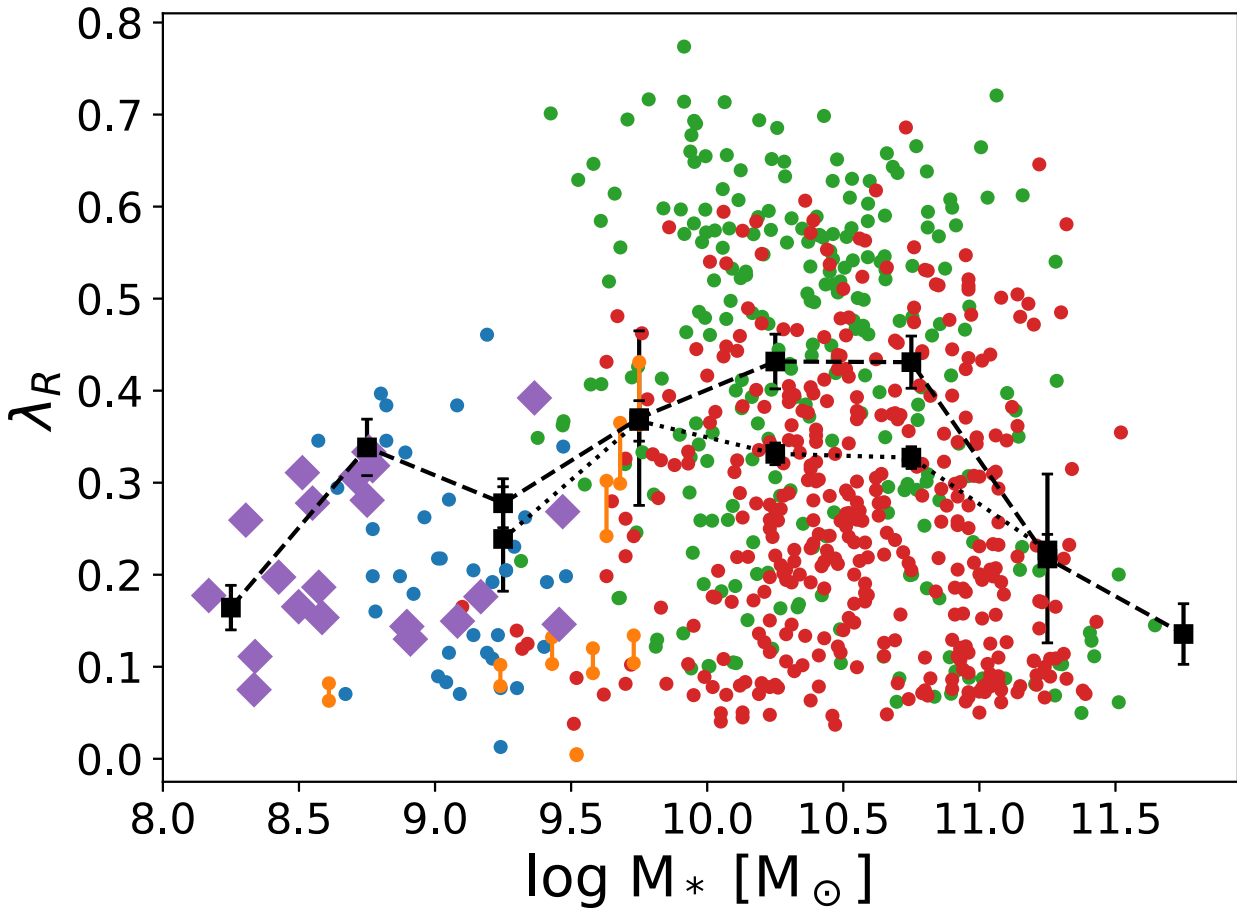
Figure 8. λ_R as a function of log $M_\star$ for galaxies with an early-type morphology. Purple points from this work, blue points from Toloba et al. (2014), orange points from Janz et al. (2017), red points from van de Sande et al. (2017), and green points from Emsellem et al. (2011). The black squares and error bars indicate the mean and error on the mean within bins of 0.5 dex in $M_\star$ for cluster (dashed) and field (dotted) subsamples, respectively.
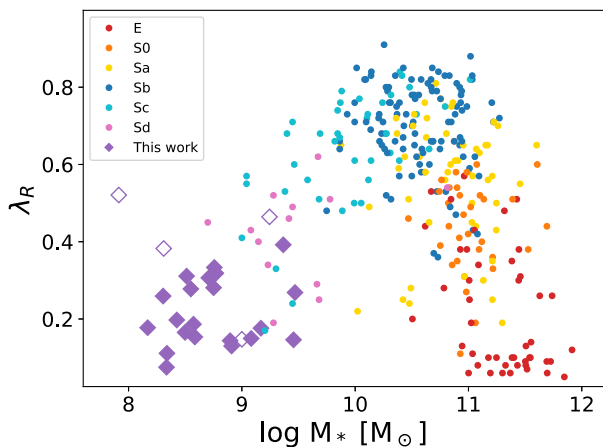

Figure 9. λ_R versus $M_\star$ for galaxies of all morphological types. Coloured points from Falcón-Barroso et al. (2019), solid purple diamonds are dEs from this work, and open purple diamonds are late-type dwarfs.

trend of decreasing λ_R with decreasing $M_\star$ for spirals seen in Falcón-Barroso et al. (2019) continues, then the dynamical gap between spirals and dEs may close at $M_\star \sim 10^8$ $M_\odot$ and no kinematic heating may be required. For low-mass galaxies, this trend is consistent with the hypothesis that dEs can originate from low-mass spirals

and irregulars, as they enter a galaxy cluster and lose their gas due to ram pressure stripping. On a kinematic basis alone, we cannot rule out different physical mechanisms causing the increase in λ_R observed in dEs and spirals; however, the similarity in other observed properties, such as their exponential surface brightness distributions, is also consistent with a common formation path (see e.g. Venhola et al. 2019). In a future paper, we will address this question in more detail.

An alternate scenario (also discussed in Ryś et al. 2014) is that the progenitors of present-day dEs were low-mass $z = 1-2$ spiral galaxies that are dynamically hotter than present-day spirals. Croom et al. (in preparation) explore the ability of a pure disc-fading scenario to explain the properties of present-day lenticular galaxies, finding that the kinematics and structure of $z \sim 0$ S0 s are consistent with passively evolved $z = 1-2$ spirals, though their results are only directly applicable at $M_\star > 10^{9.5}$ $M_\odot$. No sample of $M_\star \sim 10^8$ $M_\odot$ spiral or irregular galaxies with stellar kinematic measurements exists to directly compare possible progenitor kinematics.

7.2 The environmental dependence of dE kinematics

As noted above, there is evidence for a kinematic morphology – density relation at fixed $M_\star$ among giant galaxies. For dwarf galaxies a, similar relation may exist. In their sample of dE galaxies in the Virgo cluster, Toloba et al. (2015) found that the fraction of slow
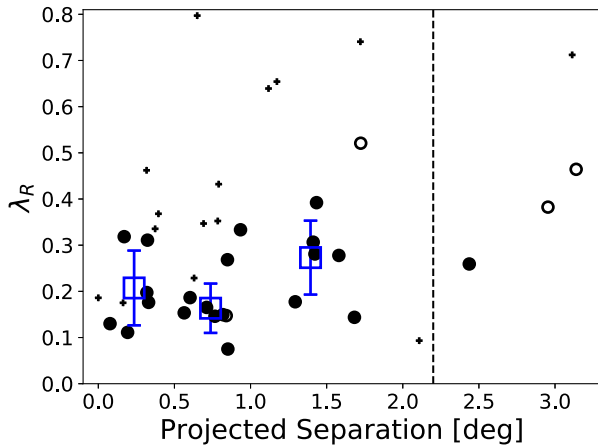
Figure 10. Specific stellar angular momentum λ_R versus distance from the centre of the cluster. Symbols as in Fig. 7. The dashed line indicates the position of the virial radius of the cluster. The blue squares and error bars indicate the mean and standard deviation for primary dE galaxies in three bins of projected separation.

rotators decreases, and the average λ_R increases, with increasing projected distance from the cluster centre. In Fig. 10, we show a consistent result for the Fornax cluster – the average λ_R of dwarf galaxies (indicated by the open blue squares) is lower in the central ~1 deg of the cluster compared to the cluster outskirts. This is consistent with the kinematic morphology – density relation found in e.g. Graham et al. (2019); however, given the relatively small sample of dE galaxies with spatially resolved kinematics, we cannot directly examine the dependence with local galaxy number density. Importantly, given our modest sample of galaxies, we cannot yet disentangle the effect of environment from the observed trends with stellar mass. We also note that Drinkwater et al. (2001a) found significant Hα emission in some dE galaxies, particularly towards the edge of the cluster, again suggesting an environmental dependence of dE properties. We will examine the emission line properties of our sample in an upcoming work.

8 CONCLUSIONS

In this work, we have presented integral field spectroscopy observations of a sample dwarf early-type galaxies in the Fornax cluster. These observations represent the largest sample of low-mass early-type galaxies in a cluster to date. We have demonstrated that our observed sample is fully representative of the dwarf galaxy population in the Fornax cluster above a stellar mass of 10^8 M$_\odot$.

For a subset of 21 dwarf early-type galaxies and four dwarf late-types, we construct maps of the spatially resolved stellar velocity and velocity dispersion. Using these maps, we assign kinematic morphological classifications to these galaxies, as well as deriving their specific stellar angular momentum, λ_R.

Combining our sample with observations of giant and massive dwarf early-type galaxies, we find that λ_R increases from the most massive galaxies to a peak around M$_\star \sim 10^{10}$ M$_\odot$, before declining towards lower masses. This is similar to the trend for slightly more massive spiral galaxies found by Falcón-Barroso et al. (2019). No comparable kinematic measurements exist for spirals of a similar mass range to our sample. Without a direct comparison sample, we cannot definitively confirm or rule out particular formation mechanisms; however, our kinematic results are consistent with a

scenario where dEs form from low-mass spiral galaxies that have their gas stripped by cluster processes, with possibly some modest external heating to fully account for dynamical differences between dEs and low-mass spirals, consistent with the findings of Koleva et al. (2014). Further observations of the stellar kinematics of star-forming dwarf galaxies are required to ascertain whether alternative formation mechanisms with increased dynamical heating are required to explain the observed kinematic differences between the two populations. We also confirm a trend first reported in Toloba et al. (2015) that the λ_R of dE galaxies is consistent with a modest increase with increasing cluster-centric radius; however, studies in a larger number of cluster and/or massive group environments are needed to solidify this result.

This paper is the first in a short series examining the dwarf early-type galaxy population of the Fornax cluster. In Eftekhari et al. (in preparation), we present the scaling relations of these galaxies and examine how the dark matter content of galaxies varies as a function of their mass. In a later paper, we will present the stellar population properties of these galaxies.

REFERENCES

Adams J. J. et al., 2014, ApJ, 789, 63
Allen J. T. et al., 2015, MNRAS, 446, 1567
Benson A. J., Toloba E., Mayer L., Simon J. D., Guhathakurta P., 2015, ApJ, 799, 171
Blakeslee J. P. et al., 2009, ApJ, 694, 556
Bland-Hawthorn J. et al., 2011, Opt. Express, 19, 2649
Boselli A., Gavazzi G., 2014, A&A Rev., 22, 74
Boselli A., Boissier S., Cortese L., Gavazzi G., 2008, ApJ, 674, 742
Bryant J. J. et al., 2015, MNRAS, 447, 2857

Bryant J. J., O'Byrne J. W., Bland-Hawthorn J., Leon-Saval S. G., 2011, MNRAS, 415, 2173

Bryant J. J., Bland-Hawthorn J., Fogarty L. M. R., Lawrence J. S., Croom S. M., 2014, MNRAS, 438, 869

Cappellari M. et al., 2007, MNRAS, 379, 418

Cappellari M., 2016, ARA&A, 54, 597

Cappellari M., Copin Y., 2003, MNRAS, 342, 345

Cappellari M., Emsellem E., 2004, PASP, 116, 138

Chilingarian I. V., 2009, MNRAS, 394, 1229

Croom S. M. et al., 2012, MNRAS, 421, 872

Davies L. J. M. et al., 2016, MNRAS, 455, 4013

Drinkwater M. J., Gregg M. D., Holman B. A., Brown M. J. I., 2001a, MNRAS, 326, 1076

Drinkwater M. J., Gregg M. D., Colless M., 2001b, ApJ, 548, L139

Emsellem E. et al., 2007, MNRAS, 379, 401

Emsellem E. et al., 2011, MNRAS, 414, 888

Falcón-Barroso J. et al., 2019, A&A, 632, A59

Ferguson H. C., Sandage A., 1990, AJ, 100, 1

Fillingham S. P., Cooper M. C., Wheeler C., Garrison-Kimmel S., Boylan-Kolchin M., Bullock J. S., 2015, MNRAS, 454, 2039

Fillingham S. P., Cooper M. C., Pace A. B., Boylan-Kolchin M., Bullock J. S., Garrison-Kimmel S., Wheeler C., 2016, MNRAS, 463, 1916

Geha M., Guhathakurta P., van der Marel R. P., 2003, AJ, 126, 1794

Geha M., Blanton M. R., Yan R., Tinker J. L., 2012, ApJ, 757, 85

Graham M. T. et al., 2018, MNRAS, 477, 4711

Graham M. T., Cappellari M., Bershady M. A., Drory N., 2019, preprint (arXiv:1910.05139)

Green A. W. et al., 2018, MNRAS, 475, 716

Gunn J. E., Gott J. Richard I., 1972, ApJ, 176, 1

Hammer F., Yang Y., Wang J., Arenou F., Puech M., Flores H., Babusiaux C., 2019, ApJ, 883, 171

Hamraz E., Peletier R. F., Khosroshahi H. G., Valentijn E. A., den Brok M., Venhola A., 2019, A&A, 625, A94

Hernquist L., 1989, Nature, 340, 687

Iodice E. et al., 2016, ApJ, 820, 42

Iodice E. et al., 2019, A&A, 627, A136

Jaffé Y. L. et al., 2018, MNRAS, 476, 4753

Janz J. et al., 2012, ApJ, 745, L24

Janz J., Penny S. J., Graham A. W., Forbes D. A., Davies R. L., 2017, MNRAS, 468, 2850

Koch A., Burkert A., Rich R. M., Collins M. L. M., Black C. S., Hilker M., Benson A. J., 2012, ApJ, 755, L13

Koleva M., De Rijcke S., Zeilinger W. W., Verbeke R., Schroyen J., Vermeylen L., 2014, MNRAS, 441, 452

Larson R. B., Tinsley B. M., Caldwell C. N., 1980, ApJ, 237, 692

Lisker T., Grebel E. K., Binggeli B., 2006, AJ, 132, 497

Lisker T., Grebel E. K., Binggeli B., Glatt K., 2007, ApJ, 660, 1186

Lisker T., Weinmann S. M., Janz J., Meyer H. T., 2013, MNRAS, 432, 1162

Mentz J. J. et al., 2016, MNRAS, 463, 2819

Michielsen D. et al., 2008, MNRAS, 385, 1374

Moore B., Lake G., Katz N., 1998, ApJ, 495, 139

Naab T. et al., 2014, MNRAS, 444, 3357

Owers M. S. et al., 2019, ApJ, 873, 52

Pedraz S., Gorgas J., Cardiel N., Sánchez-Blázquez P., Guzmán R., 2002, MNRAS, 332, L59

Peng Y.-j. et al., 2010, ApJ, 721, 193

Penny S. J. et al., 2016, MNRAS, 462, 3955

Penny S. J., Janz J., Forbes D. A., Benson A. J., Mould J., 2015, MNRAS, 453, 3635

Poggianti B. M. et al., 2017, ApJ, 844, 48

Prugniel P., Soubiran C., Koleva M., Le Borgne D., 2007, preprint (arXiv:astro-ph/0703658)

Roediger J. C. et al., 2017, ApJ, 836, 120

Ryś A., Falcón-Barroso J., van de Ven G., 2013, MNRAS, 428, 2980

Ryś A., van de Ven G., Falcón-Barroso J., 2014, MNRAS, 439, 284

Sarzi M. et al., 2018, A&A, 616, A121

Schaefer A. L. et al., 2019, MNRAS, 483, 2851

Scott N. et al., 2018, MNRAS, 481, 2299

Scott N., Davies R. L., Houghton R. C. W., Cappellari M., Graham A. W., Pimbblet K. A., 2014, MNRAS, 441, 274

Sharp R. et al., 2006, Proc. SPIE, 6269, 62690G

Sharp R. et al., 2015, MNRAS, 446, 1551

Strateva I. et al., 2001, AJ, 122, 1861

Taylor E. N. et al., 2011, MNRAS, 418, 1587

Toloba E. et al., 2014, ApJS, 215, 17

Toloba E. et al., 2015, ApJ, 799, 172

van de Sande J. et al., 2017, MNRAS, 472, 1272

Veale M. et al., 2017, MNRAS, 464, 356

Venhola A. et al., 2018, A&A, 620, A165

Venhola A. et al., 2019, A&A, 625, A143

Wetzel A. R., Tinker J. L., Conroy C., van den Bosch F. C., 2013, MNRAS, 432, 336

Wittmann C., Lisker T., Pasquali A., Hilker M., Grebel E. K., 2016, MNRAS, 459, 4450

Zabel N. et al., 2019, MNRAS, 483, 2251

SUPPORTING INFORMATION

Supplementary data are available at *MNRAS* online.

Figure S1. Images and stellar kinematic maps for all primary targets with good-quality kinematics, ordered by increasing M_r.
Figure S2. As Fig. A1, but for dwarf late-type galaxies.
Figure S3. As Fig. A1, but for giant galaxies, ordered by FCC number.
Table S1. SAMI–Fornax Dwarfs Survey secondary targets

Please note: Oxford University Press is not responsible for the content or functionality of any supporting materials supplied by the authors. Any queries (other than missing material) should be directed to the corresponding author for the article.

This paper has been typeset from a TEX/LATEX file prepared by the author.